Interplay between the mechanics of bacteriophage fibers and the strength of virus-host links

P. Ares,[1,2,3] C. Garcia-Doval,[4] A. Llauró,[2,3] J. Gómez-Herrero,[2,3] M. J. van Raaij,[4] and P. J. de Pablo[2,3,*]

[1]*Nanotec Electrónica S.L., Ronda de Poniente, 12-2 C, 28760 Tres Cantos, Madrid, Spain*

[2]*Departamento de Física de la Materia Condensada, Universidad Autónoma de Madrid, 28049 Madrid, Spain*

[3]*IFIMAC, Centro de Investigación de Física de la Materia Condensada, 28049 Madrid, Spain*

[4]*Departamento de Estructuras de Macromoléculas, Centro Nacional de Biotecnología (CNB-CSIC), calle Darwin 3, 28049 Madrid, Spain*

(Received 20 September 2013; revised manuscript received 27 January 2014; published 16 May 2014)

Viral fibers play a central role in many virus infection mechanisms since they recognize the corresponding host and establish a mechanical link to its surface. Specifically, bacteriophages have to anchor to bacteria through the fibers surrounding the tail before starting the viral DNA translocation into the host. The protein gene product (gp) 37 from bacteriophage T4 long tail fibers forms a fibrous parallel homotrimer located at the distal end of the long tail fibers. Biochemical data indicate that, at least, three of these fibers are required for initial host cell interaction but do not reveal why three and no other numbers are required. By using atomic force microscopy, we obtained high-resolution images of gp37 fibers adsorbed on a mica substrate in buffer conditions and probed their local mechanical properties. Our experiments of radial indentation at the nanometer scale provided a radial stiffness of ∼0.08 N/m and a breaking force of ∼120 pN. In addition, we performed finite element analysis and determined a Young's modulus of ∼20 MPa. From these mechanical parameters, we hypothesize that three viral fibers provide enough mechanical strength to prevent a T4 virus from being detached from the bacteria by the viral particle Brownian motion, delivering a biophysical justification for the previous biochemical data.

DOI: 10.1103/PhysRevE.89.052710 PACS number(s): 87.64.Dz, 87.15.La

I. INTRODUCTION

Mechanical properties of biological molecular aggregates are essential to their function. Indeed, forces at the nanoscale play a central role in biochemistry, from the myosin-actin system [1], which is ultimately responsible for muscle motion, to the DNA-related motor proteins [2]. Viruses are striking examples of biomolecular aggregates where recent studies of their individual mechanical properties have provided interesting insights into their physical functionalities. Among others, these studies have unveiled the structural role that the DNA may play either reinforcing the shell or exerting pressure on the viral walls [3–6], the influence of defects on their stiffnesses [7], the existence of mechanical prestress [8,9], or the dependence of the mechanical properties on the conformational changes required for the infectivity [10,11].

Together with the nucleic-acid containing capsid, a virus possesses other structures, such as the tails and the fibers, whose physical properties have not been studied yet with single molecule techniques, despite their importance in the viral cycle. Specifically, viral fibers are present in many eukaryotic viruses and bacteriophages, and they are responsible for the initial stages of infection [12]. For instance, human adenovirus fiber binds the coxsackievirus-adenovirus receptor protein, which is on the cell surface [13]. Many of the bacteriophages belonging to the *Caudovirales* order also use fiber proteins for host recognition and adhesion to the bacterial cell wall. In particular, bacteriophage T4, a *myovirus*, has been studied extensively as a model system for assembly of complex structures [14]. In the case of phage T4, the initial recognition of the bacterial cell required for the infection, is carried out by the long tail fibers [depicted in Fig. 1(a)]. These fibers reversibly bind to the outer glucose[α1-3]glucose region of the bacterial lipopolysaccharide (LPS) or the outer membrane porin C [15,16]. Upon receipt of the signal—achieved when, at least, three long tail fibers have encountered suitable receptors—a conformational change in the baseplate [17] allows the short tail fibers, which are trimers of gene product (gp) 12, to extend [18]. Once these short tail fibers have irreversibly bound the core region of the LPS [19], a conformational change likely allows the inner tail tube to pass through the baseplate (an action driven by the contraction of the outer tail sheath). Phage proteins and DNA can then enter the bacteria and can initiate infection which, in favorable conditions, can lead to several hundred daughter phages and bacterial lysis within 30 min [20].

The long tail fiber can be divided in proximal and distal halves, each over 70 nm long and connected at an angle of about 160° [21]. The half proximal to the phage (the thigh) is made up of a trimer of gp34, a 1289 amino acid protein of unknown structure. At the kink, a single copy of gp35 (372 residues) is located. The top of the shin is constructed of a trimer of the 221 amino acid protein gp36, whereas, the major part of the shin and the receptor-binding tip (or foot) is composed of a parallel homotrimer of gp37. A long tail fiber structure is shown in Fig. 1(b). Full-length gp37 contains 1026 residues. The crystal structure of a trimer containing residues 811–1026 for each of the three chains has been resolved at a 2.2 Å resolution [22]. The structure revealed a collar domain similar to that observed for gp12 [23], which is composed of amino acids 811–861 plus a β strand formed by the very carboxyl terminus of the protein (residues 1016–1026). This means the amino and carboxyl termini of this fragment are close, and the intervening residues form an extensively interwoven and intertwined region [Fig. 1(b)] (residues 862–880 plus 1009–1015), a needle domain consisting of amino acids 881–933 plus 960–1008 and a small head domain formed

*p.j.depablo@uam.es

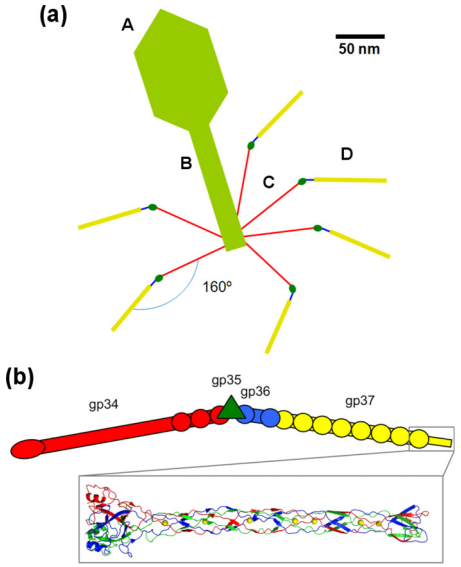

FIG. 1. (Color online) A fiber's structure. (a) shows the relative position of gp37 fibers—yellow (thicker) lines—in phage T4: *A*: virus capsid; *B*: inner tail; *C*: proximal half fibers; *D*: distal half fibers. $C + D$ long tail fibers. (b) shows the long tail fibers' structure and protein domains. The detail in the rectangle shows the known crystallographic structure of the gp37 fiber.

by residues 934–959. The head domain is responsible for initial host recognition. Since, at least, three fibers have to hold the capsid onto the bacterial cell wall, their mechanical strength must, at least, overcome the mechanical tension provided by the thermal Brownian motion of the virus. We report herein on the mechanical properties of gp37 fibers, such as the Young's modulus, the breaking force and stiffness, which we have obtained by atomic force microscopy (AFM) and finite element analysis (FEA). We relate these data with the mechanical function of the fibers during the first stage of viral infection, providing a hypothesis of why, at least, three fibers are needed to initiate T4 infection.

II. MATERIALS AND METHODS

A. Sample preparation

For purification of amino-terminally six-histidine tagged gp37 containing residues 12–1026, cultures of JM109(DE3) transformed with pCDF (Sm)gp37 and pET(Ap)57 were grown at 37 °C in Luria Broth medium supplemented with ampicillin (100 mg/l) and streptomycin (50 mg/l) to an optical density of 0.6 units measured at 600 nm [24]. Expression was induced by adding isopropyl-β-D-thiogalactoside to a final concentration of 1 mM, and growth was continued overnight at 16 °C. Bacteria were harvested by centrifugation, and pellets were resuspended in a lysis buffer (50 mM Tris-HCl pH 8.0, 4% (v/v) glycerol, 50 mM ammonium chloride, 2 mM ethylenediaminetetraacetic acid and 150 mM sodium chloride). Cells were lysed by ten rounds of 10 s sonications alternated with incubation on ice, and extracts were centrifuged for 20 min at 20 000 × g at 4 °C. Imidazole from a 1M stock at pH 7.0 was added to the supernatants to give a final concentration of 50 mM, and the resulting mixture was loaded onto a nickel-iminodiacetic acid agarose column equilibrated in buffer A (50 mM Tris-HCl pH 8.5; 300 mM sodium chloride) containing 50 mM imidazole. One milliliter resin slurry as supplied (Jena Bioscience, Jena, Germany) was used to form the column. Elution was performed with six passes of 5 ml of buffer A containing 100, 150, 200, 250, 300, and 400 mM imidazole, respectively. The 150, 200, and 250 mM imidazole fractions were combined and were dialyzed against 10 mM Tris-HCl pH 8.5. The protein was applied to a 6 ml Resource Q column equilibrated with 10 mM Tris-HCl pH 8.5 and eluted with a sodium chloride gradient. Highly purified protein eluted at around 0.25 M sodium chloride was dialyzed against 10 mM Tris-HCl pH 8.5. A stock of purified gp37 fibers at 0.1 mg/ml in 10 mM Tris-HCl buffer at pH 8.5 was used.

B. Atomic force microcopy

For AFM experiments, the stock solution was diluted 20 × to 5 μg/ml. To attach the fibers to the substrates, surfaces of freshly cleaved mica disks were immersed in a solution of 0.1% of 3-aminopropyl-triethoxy-silane (Sigma-Aldrich). Then the mica disks were rinsed with 2-propanol and water and were dried in a N_2 gas jet. A 40 μl drop of diluted stock was deposited onto a treated mica disk. The drop was left on the surface for 20 min and, afterwards, was rinsed four times with a 40 μl drop of buffer without allowing surface dewetting. The tip also was prewetted with a 30 μl drop of buffer solution in order to perform the experiments in the liquid. A Cervantes Fullmode AFM (Nanotec Electrónica, Madrid, Spain, www.nanotec.es) was operated in the buffer at room temperature using the noncontact dynamic mode [25] through the WSXM software [26]. A cantilever holder specially designed to work in this mode in liquid environments was used [27] to guarantee an optimum operation of the microscope. We used silicon nitride rectangular cantilevers (OMCL-AC40TS; Olympus, Tokyo, Japan, http://probe.olympus-global.com). The spring constants of the four different cantilevers used for the measurements were calibrated by using Sader's method in air [28], yielding 0.06 ± 0.01 N/m with an average tip radius of 11 nm [29] [Supplemental Material (SM) [30], Fig. S1] and resonance frequency values in buffer conditions of ∼20 kHz. Low spring constant cantilevers were chosen due to their high force sensitivity, which is convenient for soft samples.

The cantilevers were oscillated with amplitudes of ∼3 nm at their resonance frequency. In order to minimize the tip-sample interaction and increase the scan rate, images were only acquired while the tip was scanning from left to right (trace). The retrace was acquired much faster but with the tip far away from the surface. AFM images and spectroscopy data were processed by using the WSXM software. After locating individual fibers on the surface, the selected sample was zoomed in, and the scan was performed always on the same line with the fiber filling near the whole image range. Then the lateral scanning was stopped when the tip was on top of the fiber. At this point, a force vs z-piezo (FZ) position curve was performed by elongating the z-piezo so that the tip established mechanical contact with the fiber (nanoindentation). After each FZ measurement, the fiber immediately was scanned to check for structural integrity. Thus, about two or three

consecutive nanoindentation-imaging cycles were performed on the fiber until a breakage event was observed in both indentation curve and AFM topography.

C. Young's modulus calculations with FEA

To calculate the Young's modulus values from FZ curves, these data had to be converted into force vs indentation $F(\delta)$ curves. This standard process consists of comparing the measured FZ curve on the sample with the FZ curve on the substrate (mica in our case). At any applied force value, the corresponding difference in the z distance between the FZ curves provides a measure of the fiber's indentation at that force value [31]. The resulting indentation curve can be fitted to physics-based models that predict the AFM tip-sample contact mechanics, and the Young's modulus can be estimated by tuning the theoretical Young's modulus value to match the theoretical prediction with the experimental data [32,33].

FEA was performed using COMSOL MULTIPHYSICS 4.1. The viral fiber was made of a homogenous material (SM [30], Fig. S2) with a Poisson ratio of 0.3 according to studies with similar conditions [9,34,35] and taking into account that previous FEA on viral capsids showed that the models were quite insensitive to the Poisson ratio variation [36]. The viral fiber was modeled mimicking the dimensions and geometry of the fiber structure obtained from electron microscopy (EM) volume data [21]. The fiber was placed on a flat rigid surface and was loaded with a rigid 11 nm radius indenter, similar to the AFM tips used in our experiments. The contacts between the fiber and the tip and between the fiber and the surface were both implemented with a contact-penalty stiffness method according to the COMSOL manual. Considering the symmetry of the geometry, the model was reduced to one half and was meshed over 6801 tetrahedral elements. A parametric nonlinear solver was used to simulate the stepwise lowering of the indenter onto the fiber. To match the experimental curves with the simulation, the Young's modulus was varied until accordance between simulation and experiment successfully was reached.

D. Brownian force of phage T4

Assuming that the shape of the T4 can be approximated by a sphere of radius $r \sim 50$ nm, its dragging coefficient is given by Stoke's law as $\gamma = 6\pi\eta r = 9.4 \times 10^{-10}$ N s m^{-1}, where η is the water viscosity (0.001 Pa s) [37,38]. As a consequence of the principle of equipartition, the root mean square virus velocity at room temperature T is given by $\langle v^2\rangle^{1/2} = (\frac{3k_BT}{m})^{1/2} = 0.20$ m/s, where k_B is the Boltzmann constant and m is the mass of the phage T4 ($\sim$190 MDa) [39]. The persistence time τ, that represents the lag in time in which the virus moves in a given direction due to the thermal power stroke is given by $\tau = \frac{m}{\gamma} = 335$ ps. On average, during this time, the virus particle moves a distance $d = v \times \tau = 0.7$ Å in a random direction, which represents about $\sim 1/1400$ of the phage diameter. The variance in the power spectrum of the thermal force of a tethered virus is independent of the frequency and only depends on the drag coefficient and not on the stiffness of the tether, i.e., $\langle F^2\rangle = \gamma^2\langle v^2\rangle$ [40]. From this formula and the standard deviation of the velocity provided by the Maxwell-Boltzmann distribution of velocities, i.e., $\sigma = \sqrt{(\frac{3\pi-8}{\pi})(\frac{k_BT}{m})}$, we derive the force for every thermal shake on the viral particle to be $F_{\text{thermal}} \sim 190 \pm 70$ pN.

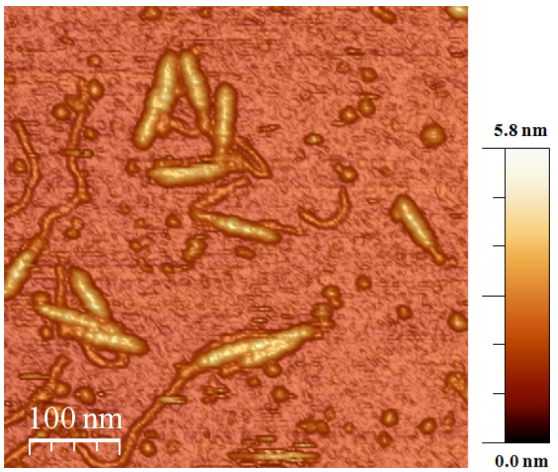

FIG. 2. (Color online) gp37 fibers on mica. This topographical AFM image represents a random population of gp37 fibers on mica under buffer conditions.

III. RESULTS

After fibers have anchored to the substrate dynamic AFM imaging of the surface in buffer conditions reveals a random dispersion of elongated structures (Fig. 2). Each of them shows several longitudinal bumps which correspond fairly well to the different protein modules composing the gp37 viral fibers [Fig. 3(a)] [22].

An inherent effect of AFM imaging of samples with a similar dimension to the tip radius is the increase in lateral size, although the height remains unchanged. Thus, we can analyze the topography of the fibers by calculating the expected geometrical dilation effect between the tip and the proteins. Models of the gp37 fibers were created based on the EM volume of the fibers [21]. Therefore, we processed the fibers' EM data [Fig. 3(a)] with a dilation algorithm using a parabolic tip ($z = x^2/2r$) [41]. For the radius r, we chose 11 nm. The resulting dilated fiber [Fig. 3(b)] presents topographical features in good agreement with the AFM image of Fig. 3(c). Processed data reveal that the fiber width is highly affected by dilation. Conversely, since the fiber is much longer than the tip radius, its length remains unchanged by the lateral dilation. We have measured the height and the length of 55 viral fibers, obtaining an average height of 4.7 ± 0.3 nm (5.1 ± 0.3 and 4.3 ± 0.3 nm for the protein moduli and interprotein moduli loci, respectively) and a length of 64 ± 5 nm (SM [30], Fig. S3), both in good agreement with the dimensions expected from the fiber proteins and from previous EM data [Fig. 3(a)] [21,24]. The comparison of the height profiles along the fiber between EM and AFM data [Fig. 3(d)] also indicates a reasonable match, bearing in mind that the EM volume is the result of averaging images of many fibers, whereas the AFM volume is the result of scanning only one fiber.

For the indentation experiments, once a single fiber is selected on the surface, we perform a nanoindentation on its

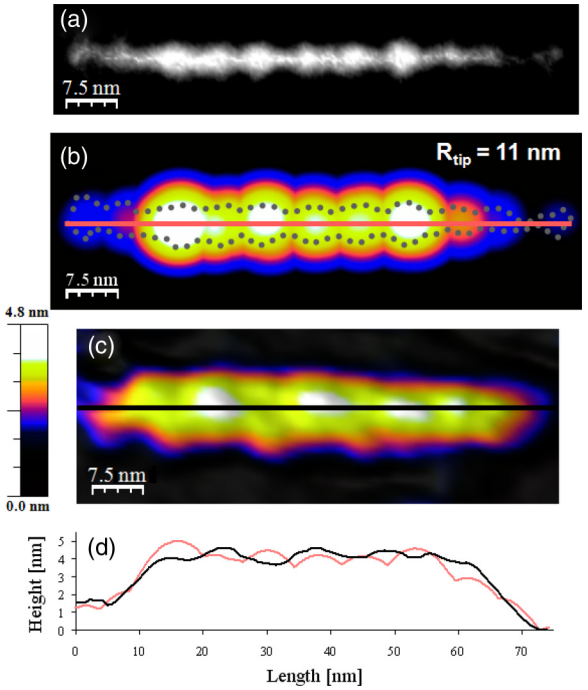

FIG. 3. (Color online) Topographic analysis and EM-AFM data comparison. (a) presents EM volume data of gp37 [21]. (b) shows a geometrical dilation filtering of EM data with a tip of radius 11 nm. The dotted contour highlights the EM data for the sake of comparison. (c) presents experimental topographical AFM data of a gp37 fiber adsorbed on mica. Horizontal profiles in (b) red (light gray) and (c) black are depicted in (d).

top. Afterwards, an image of the fiber is acquired to check its integrity (see Materials and Methods). The procedure is repeated until the fiber is broken. Figure 4 presents the AFM image of a fiber before [Fig. 4(a)] and after [Fig. 4(b)] the dismantling provoked by the FZ of Fig. 4(c). Figure 4(b) demonstrates the dramatic modification caused by the nanoindentation curve as we observe that several protein moduli have been ripped out by the tip. The mechanism of the fiber indentation [Fig. 4(c)] is performed as follows: after taking a reference FZ on mica (black), the cantilever approaches the fiber at zero deflection until it establishes mechanical contact. Afterwards, the tip starts deforming the fiber, showing a linear deformation from point *A* to point *B* where a steep drop in the cantilever indicates that the fiber is broken and the tip taps the mica surface.

Figure 5(a) presents 18 indentation curves performed on 18 different fibers where the surface deflection signal has previously been subtracted from the fiber deflection one in order to obtain the deformation of the fiber [31,42]. To this end, it is assumed that, although the tip can squeeze the fiber, it cannot deform the surface of the substrate (the substrate stiffness is much greater than the cantilever force constant). The contact point between the tip and the fiber is determined by the change in the force slope and the subsequent force noise reduction. While the tip approached the fiber, the cantilever was free and no force was measured, but when the tip reached the top of the fiber, indentation started, the slope of the curves changed abruptly, and the force noise decreased [43]. By

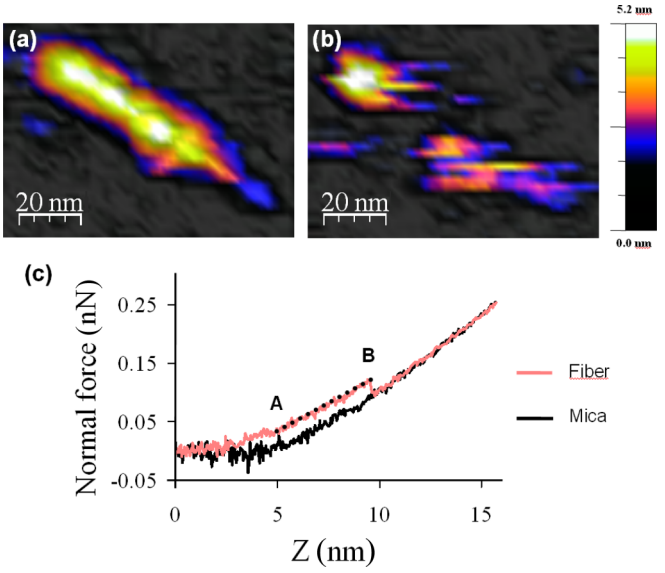

FIG. 4. (Color online) Breaking a gp37 fiber. (a) and (b) present the topographical images of a fiber before and after a nanoindentation experiment. Forward cycles of nanoindentation on the fiber and on the mica substrate are depicted in (c) red (light gray) and black, respectively. Point *A:* marks the starting point of the linear deformation of the fiber. The dotted line depicts the linear fit for extracting the stiffness of the fiber. Point *B*: the fiber is broken.

shifting the indentation curves to coincide with the tip-fiber contact points of all the curves, we can observe a variety in the distance indented until the substrate is reached by the tip. Most of the indentation ranges from about 4 to 5 nm in good

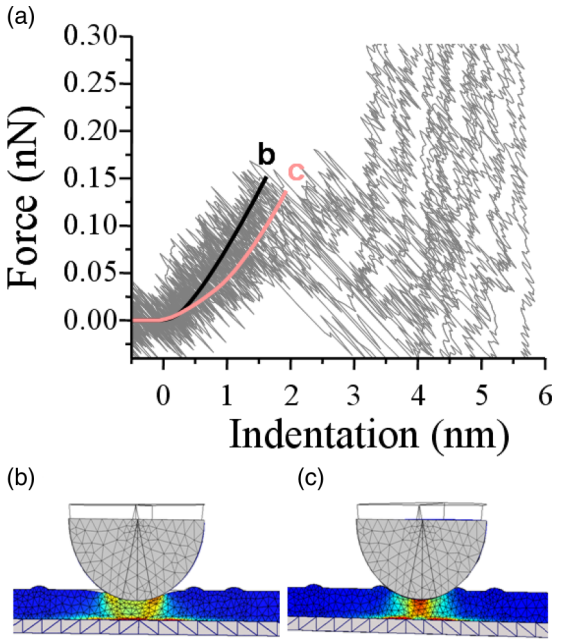

FIG. 5. (Color online) Indentation curves on gp37 and FEA. (a) presents 18 indentation graphs pertaining to 18 different fibers and the data fits from the FEA: (b) black for the tip indenting on a protein moduli and (c) red (light gray) for the tip indenting on an interprotein moduli.

agreement with FZs performed at interprotein modulus loci and at top of a protein modulus (SM [30], Fig. S3).

Figures 5(b) and 5(c) show FEA simulations corresponding to the tip indenting at the interprotein modulus and at the top of the protein modulus loci.

IV. DISCUSSION

It is instructive to estimate the approximate viral fiber stiffness by considering both cantilever and fiber as two springs in series with spring constants k_{cl} and $k_{fib,}$ respectively, thus, obtaining [6]

$$\frac{1}{k_{ms}} = \frac{1}{k_{cl}} + \frac{1}{k_{fib}}, \tag{1}$$

where k_{ms} is the spring constant measured from point A to point B in a nanoindentation event [Fig. 4(c)] that accounts for simultaneous deformations of the cantilever and the fiber. Assuming a linear deformation, we estimate an average gp37 fiber's radial stiffness of $k_{fib} = 0.08 \pm 0.03$ N/m, similar to other bacteriophage bodies, such as phi29 [9].

To perform a more profound mechanical characterization of the fibers, FEA of the tip-fiber system has been performed (Materials and Methods) to estimate the Young's modulus of the fibers. Figure 5(a) shows the experimental data corresponding to indentations randomly distributed along 18 fibers and the FEA fits corresponding to two boundary cases: the tip indenting on the top of a protein modulus [Fig. 5(b)] and on an interprotein modulus [Fig. 5(c)]. The comparison between the indentation experiments and the aforementioned cases of the simulation results in a value of the Young's modulus of the fiber $E_{fib} = 20 \pm 5$ MPa.

Using the obtained Young's modulus, we can calculate the longitudinal stiffness of the fibers. From Hooke's law, the stiffness of an isotropic cylinder along its main axis can be expressed as follows:

$$k_{fib} = \frac{E_{fib} A_0}{L_0}, \tag{2}$$

where A_0 is the cross section through which the force is applied and L_0 is the length of the object. Figure 1(b) illustrates that the homotrimer forms an extensively interwoven intertwined region where the three proteins are heavily coupled. Therefore, in first approximation, as commonly performed in such kinds of analyses, we can assume the fibers as isotropic cylinders [33,44] (SM [30], Fig. S2) where A_0 will be the cross-sectional area of the fibers and L_0 will be their length. Thus, the longitudinal stiffness results in $k_{long} = 0.005 \pm 0.002$ N/m.

The experiments also allow us to extract other important mechanical parameters, such as the radial breaking force $F_{rad} = 120 \pm 30$ pN and a collapse distance of 2.0 ± 0.3 nm (SM [30], Fig. S4). From both the FEA and the Hertz model (SM [30]), we can extract the average area of contact between the tip and the fiber at the radial breaking force to be $s = 13.5 \pm 1.5$ nm^2 and can derive a tensile strength of $\sigma_r = \frac{F_{rad}}{s} = 9$ MPa. The fiber cross section A_0 is calculated by using its semiheight (see Results) as the average radius to give 17 nm^2. Thus, assuming isotropy, we can estimate the longitudinal breaking force $F_{long} = \sigma_r \times A_0 = 150 \pm 30$ pN.

We can compare our results with other protein fibers [45]. In particular, fibrin fibers, which are the major structural component of a blood clot, are extraordinarily extensible and elastic, and they are relatively soft [46–48]. Although fibrin fibers' lengths and diameters are much larger than gp37 fibers, fibrin fibers are assembled from fibrin monomers, which come from the removal of two pairs of fibrinopeptides in the fibrinogen. Fibrinogen is a highly abundant soluble plasma protein, and it is 46 nm in length and 4.5 nm in diameter [49], which are similar to the gp37 fibers' dimensions. The Young's modulus and the rupture force per monomer of fibrin fibers are 1–10 MPa [46,48,50] and 280 pN [47], respectively. Since the Young's modulus is a bulk material property, it is not surprising that fibrin fibers show similar values to gp37 fibers because the ultimate building blocks of both structures are individual proteins.

On the other hand, it is convenient to discuss the biophysical implications of our results. T4 phage infection is initiated by the attachment of, at least, three long tail fibers to the host [51]. This process triggers a conformational change in the baseplate that induces the tail expansion and the subsequent DNA translocation into the host [38]. During this process, long tail fibers have to withstand detaching forces, such as those caused by the Brownian fluctuations, the mechanical tensions derived from the multiple conformational changes occurring during infection, or the exchange of momentum provided by the DNA translocation. In particular, the mechanical resistance of the first three bound fibers against the thermal shaking of the viral particle is critical for infectivity. The thermally activated Brownian motion of a viral particle consists of random displacements of a distance $d \sim 0.7$ Å every 300 ps on average (Materials and Methods). When the virus is pulled normally from the bacteria surface by thermal vibrations, both fiber and fiber receptor are subjected to an average force $F_{thermal} = 190 \pm 70$ pN (Materials and Methods). We can compare $F_{thermal}$ with the longitudinal breaking force of a fiber F_{long} to hypothesize about why, at least, three fibers are required for initiating T4 infection. By accounting the phage fibers as parallel tethers anchoring the viral particle to the bacteria wall, we can estimate the breaking force for one to three fibers (Fig. 6). We find that one and two fibers are insufficient to hold the virus particle on the bacteria, and only three or more fibers provide enough resistance to the thermal force.

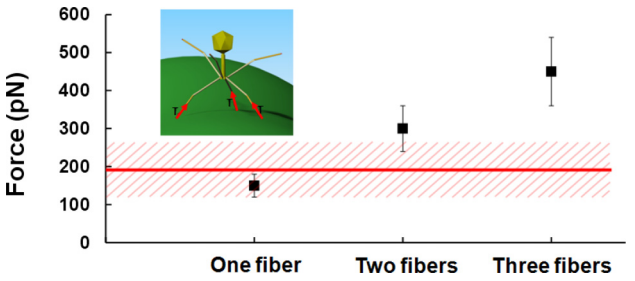

FIG. 6. (Color online) Thermal force and fibers breaking forces. The horizontal red line depicts the thermal force $F_{thermal}$ of the T4 bacteriophage 190 ± 70 pN. Squares represent the forces needed to break one to three fibers. Inset: The cartoon of a T4 virus attached to a bacterium through three of its long tail fibers, showing the tension on each of them during a thermal power stroke.

After recognition has occurred and the virus is bound to the bacteria, a variety of conformational changes allows the short tail fibers to bind to the outer region of the bacterial lipopolysaccharide and the inner tail tube to pass through the baseplate. As a consequence of these conformational changes, the long and short tail fibers, together with the tube of the tail, hold the virus attached to the bacteria, and the DNA translocation starts, exerting a force of ∼60 pN [52]. The longitudinal breaking force of an individual long tail fiber (∼150 pN) is about twice the force induced by DNA translocation. Thus, the three fibers do not only withstand the force induced by thermal shaking during the fiber-host recognition stage, but also the forces during the rest of the infection process.

V. CONCLUSIONS

We have obtained high-resolution AFM images of the bacteriophage T4 gp37 fibers under close to physiological conditions. By using radial indentations together with finite element analysis, we have determined fibers' Young's modulus (20 MPa), radial stiffness (0.08 N/m), and radial and longitudinal breaking forces (120 and 150 pN, respectively). With these results, we estimated the mechanical resistance of the fibers to hold the viral particle on the bacteria of being detached by Brownian motion. Thus, we hypothesized that three fibers provide enough mechanical resistance for initiating the infection. These results and further studies, such as, for example, the use of bacterial lipopolysaccharide and isolated outer membrane porin C or the performance of pulling experiments, could lead to a better understanding of the mechanical basis of viral-host recognition and infection mechanisms.

ACKNOWLEDGMENTS

We acknowledge funding from Grants No. MAT2008-02533, No. PIB2010US-00233, No. FIS2011-29493, and No. FIS2011-16090-E (P.J.deP.), No. BFU2008-01588, No. BFU2011-24843, and No. BIO2011-14756-E (M.J.vR) from the Spanish Ministry of Economy and Competitiveness, an FPU Ph.D. fellowship from the Ministry of Education (C.G.-D.) and the Red Española Interdisciplinar de Biofísica de los Virus (BioFiViNet). We also thank A. Gil and M. Hernando-Pérez for insightful discussions and F. J. García-Vidal for the help with the finite element analysis.

[1] K. Shiroguchi and K. Kinosita, Science **316**, 1208 (2007).
[2] F. Moreno-Herrero, M. de Jager, N. H. Dekker, R. Kanaar, C. Wyman, and C. Dekker, Nature (London) **437**, 440 (2005).
[3] C. Carrasco, A. Carreira, I. A. T. Schaap, P. A. Serena, J. Gomez-Herrero, M. G. Mateu, and P. J. de Pablo, Proc. Natl. Acad. Sci. USA **103**, 13706 (2006).
[4] C. Carrasco, M. Castellanos, P. J. de Pablo, and M. G. Mateu, Proc. Natl. Acad. Sci. USA **105**, 4150 (2008).
[5] M. Hernando-Perez, R. Miranda, M. Aznar, J. L. Carrascosa, I. A. T. Schaap, D. Reguera, and P. J. de Pablo, Small **8**, 2366 (2012).
[6] I. Ivanovska, G. Wuite, B. Jonsson, and A. Evilevitch, Proc. Natl. Acad. Sci. USA **104**, 9603 (2007).
[7] W. H. Roos, K. Radtke, E. Kniesmeijer, H. Geertsema, B. Sodeik, and G. J. L. Wuite, Proc. Natl. Acad. Sci. USA **106**, 9673 (2009).
[8] M. Baclayon, G. K. Shoemaker, C. Uetrecht, S. E. Crawford, M. K. Estes, B. V. V. Prasad, A. J. R. Heck, G. J. L. Wuite, and W. H. Roos, Nano Lett. **11**, 4865 (2011).
[9] C. Carrasco *et al.*, Biophys. J. **100**, 1100 (2011).
[10] M. Castellanos, R. Perez, C. Carrasco, M. Hernando-Perez, J. Gomez-Herrero, P. J. de Pablo, and M. G. Mateu, Proc. Natl. Acad. Sci. USA **109**, 12028 (2012).
[11] A. Ortega-Esteban, A. J. Pérez-Berná, R. Menéndez-Conejero, S. J. Flint, C. San Martín, and P. J. de Pablo, Sci. Rep. **3**, 1434 (2013).
[12] J. Carter and V. Saunders, *Virology: Principles and Applications* (Wiley, Hoboken, NJ, 2007).
[13] M. C. Bewley, K. Springer, Y. B. Zhang, P. Freimuth, and J. M. Flanagan, Science **286**, 1579 (1999).
[14] Y. Kikuchi and J. King, J. Supramol. Struct. **3**, 24 (1975).
[15] P. Prehm, B. Jann, K. Jann, G. Schmidt, and S. Stirm, J. Mol. Biol. **101**, 277 (1976).
[16] F. Yu and S. Mizushima, J. Bacteriol. **151**, 718 (1982).
[17] M. G. Rossmann, V. V. Mesyanzhinov, F. Arisaka, and P. G. Leiman, Curr. Opin. Struct. Biol. **14**, 171 (2004).
[18] P. G. Leiman, P. R. Chipman, V. A. Kostyuchenko, V. V. Mesyanzhinov, and M. G. Rossmann, Cell **118**, 419 (2004).
[19] I. Riede, Mol. Gen. Genet. **206**, 110 (1987).
[20] J. D. Karam, K. N. Kreuzer, and D. H. Hall, in *Molecular Biology of Bacteriophage T4*, edited by J. D. Karam (ASM, Washington, D.C., 1994).
[21] M. E. Cerritelli, J. S. Wall, M. N. Simon, J. F. Conway, and A. C. Steven, J. Mol. Biol. **260**, 767 (1996).
[22] S. G. Bartual, J. M. Otero, C. Garcia-Doval, A. L. Llamas-Saiz, R. Kahn, G. C. Fox, and M. J. van Raaij, Proc. Natl. Acad. Sci. USA **107**, 20287 (2010).
[23] M. J. van Raaij, G. Schoehn, M. R. Burda, and S. Miller, J. Mol. Biol. **314**, 1137 (2001).
[24] S. G. Bartual, C. Garcia-Doval, J. Alonso, G. Schoehn, and M. J. van Raaij, Protein Expression Purif. **70**, 116 (2010).
[25] F. Moreno-Herrero, P. J. de Pablo, J. Colchero, J. Gomez-Herrero, and A. M. Baro, Surf. Sci. **453**, 152 (2000).
[26] I. Horcas, R. Fernández, J. M. Gómez-Rodríguez, J. Colchero, J. Gómez-Herrero, and A. M. Baro, Rev. Sci. Instrum. **78**, 013705 (2007).
[27] C. Carrasco, P. Ares, P. J. de Pablo, and J. Gómez-Herrero, Rev. Sci. Instrum. **79**, 126106 (2008).
[28] J. E. Sader, J. Appl. Phys. **84**, 64 (1998).
[29] P. Markiewicz and M. C. Goh, Langmuir **10**, 5 (1994).
[30] See Supplemental Material at http://link.aps.org/supplemental/10.1103/PhysRevE.89.052710 for tip radii estimation, fiber homogeneity and statistics on fiber dimensions and mechanical properties.
[31] H. J. Butt, B. Cappella, and M. Kappl, Surf. Sci. Rep. **59**, 1 (2005).

[32] R. R. Lahiji, X. Xu, R. Reifenberger, A. Raman, A. Rudie, and R. J. Moon, Langmuir **26**, 4480 (2010).
[33] Y. Zhao, Z. B. Ge, and J. Y. Fang, Phys. Rev. E **78**, 031914 (2008).
[34] M. Radmacher, M. Fritz, J. P. Cleveland, D. A. Walters, and P. K. Hansma, Langmuir **10**, 3809 (1994).
[35] E. P. S. Tan and C. T. Lim, Appl. Phys. Lett. **87**, 123106 (2005).
[36] M. M. Gibbons and W. S. Klug, Phys. Rev. E **75**, 031901 (2007).
[37] A. Fokine, P. R. Chipman, P. G. Leiman, V. V. Mesyanzhinov, V. B. Rao, and M. G. Rossmann, Proc. Natl. Acad. Sci. USA **101**, 6003 (2004).
[38] P. G. Leiman, F. Arisaka, M. J. van Raaij, V. A. Kostyuchenko, A. A. Aksyuk, S. Kanamaru, and M. G. Rossmann, Virol. J. **7**, 355 (2010).
[39] S. B. Dubin, G. B. Benedek, F. C. Bancroft, and D. Freifelder, J. Mol. Biol. **54**, 547 (1970).
[40] J. Howard, *Mechanics of Motor Proteins and the Cytoskeleton* (Sinauer, Sunderland, MA, 2001).
[41] J. S. Villarrubia, J. Res. Natl. Inst. Stand. Technol. **102**, 425 (1997).
[42] P. J. de Pablo, I. A. T. Schaap, F. C. MacKintosh, and C. F. Schmidt, Phys. Rev. Lett. **91**, 098101 (2003).
[43] J. F. Graveland-Bikker, I. A. T. Schaap, C. F. Schmidt, and C. G. de Kruif, Nano Lett. **6**, 616 (2006).
[44] I. A. T. Schaap, C. Carrasco, P. J. de Pablo, F. C. MacKintosh, and C. F. Schmidt, Biophys. J. **91**, 1521 (2006).
[45] M. Guthold, W. Liu, E. A. Sparks, L. M. Jawerth, L. Peng, M. Falvo, R. Superfine, R. R. Hantgan, and S. T. Lord, Cell Biochem. Biophys. **49**, 165 (2007).
[46] J. P. Collet, H. Shuman, R. E. Ledger, S. T. Lee, and J. W. Weisel, Proc. Natl. Acad. Sci. USA **102**, 9133 (2005).
[47] W. Liu, C. R. Carlisle, E. A. Sparks, and M. Guthold, J. Thromb. Haemost. **8**, 1030 (2010).
[48] W. Liu, L. M. Jawerth, E. A. Sparks, M. R. Falvo, R. R. Hantgan, R. Superfine, S. T. Lord, and M. Guthold, Science **313**, 634 (2006).
[49] C. E. Hall and H. S. Slayter, J. Biophys. Biochem. Cytol. **5**, 11 (1959).
[50] A. E. X. Brown, R. I. Litvinov, D. E. Discher, and J. W. Weisel, Biophys. J. **92**, L39 (2007).
[51] J. T. Crawford and E. B. Goldberg, J. Mol. Biol. **139**, 679 (1980).
[52] D. N. Fuller, D. M. Raymer, V. I. Kottadiel, V. B. Rao, and D. E. Smith, Proc. Natl. Acad. Sci. USA **104**, 16868 (2007).